remote sensing

MDPI

Article

Optimized Landslide Susceptibility Mapping and Modelling Using the SBAS-InSAR Coupling Model

Xueling Wu [1,2,*], Xiaoshuai Qi [1], Bo Peng [1] and Junyang Wang [1]

[1] School of Geophysics and Geomatics, China University of Geosciences, Wuhan 430074, China; 1202220642@cug.edu.cn (X.Q.); plumbumer@cug.edu.cn (B.P.); 16-dk-wjy@cug.edu.cn (J.W.)
[2] Key Laboratory of Urban Land Resources Monitoring and Simulation, Ministry of Natural Resources, Shenzhen 518034, China
* Correspondence: wuxl@cug.edu.cn

Abstract: Landslide susceptibility mapping (LSM) can accurately estimate the location and probability of landslides. An effective approach for precise LSM is crucial for minimizing casualties and damage. The existing LSM methods primarily rely on static indicators, such as geomorphology and hydrology, which are closely associated with geo-environmental conditions. However, landslide hazards are often characterized by significant surface deformation. The Small Baseline Subset-Interferometric Synthetic Aperture Radar (SBAS-InSAR) technology plays a pivotal role in detecting and characterizing surface deformation. This work endeavors to assess the accuracy of SBAS-InSAR coupled with ensemble learning for LSM. Within this research, the study area was Shiyan City, and 12 static evaluation factors were selected as input variables for the ensemble learning models to compute landslide susceptibility. The Random Forest (RF) model demonstrates superior accuracy compared to other ensemble learning models, including eXtreme Gradient Boosting, Logistic Regression, Gradient Boosting Decision Tree, and K-Nearest Neighbor. Furthermore, SBAS-InSAR was utilized to obtain surface deformation rates both in the vertical direction and along the line of sight of the satellite. The former is used as a dynamic characteristic factor, while the latter is combined with the evaluation results of the RF model to create a landslide susceptibility optimization matrix. Comparing the precision of two methods for refining LSM results, it was found that the method integrating static and dynamic factors produced a more rational and accurate landslide susceptibility map.

Keywords: ensemble learning; SBAS-InSAR; landslide susceptibility mapping; ground surface deformation rate

Citation: Wu, X.; Qi, X.; Peng, B.; Wang, J. Optimized Landslide Susceptibility Mapping and Modelling Using the SBAS-InSAR Coupling Model. *Remote Sens.* **2024**, *16*, 2873. https://doi.org/10.3390/rs16162873

Academic Editor: Michele Saroli

Received: 20 May 2024
Revised: 28 July 2024
Accepted: 2 August 2024
Published: 6 August 2024

1. Introduction

Landslides are acknowledged as significant natural disasters on a global scale, exerting substantial impacts on both societal security and the environment [1–3]. The data demonstrate that landslides displace tens of thousands of individuals annually, resulting in substantial economic losses totaling hundreds of millions of dollars [4–6]. Among these, Latin America is geographically situated near the confluence of the American and Antarctic plates. As a result, the region experiences recurrent seismic activity and significant crustal movements, often leading to substantial landslides [7]. In the Santa Marta region, a geological event occurred in 1986, causing soil subsidence and landslides. This incident resulted in the destruction of over 100 residential structures located along the canyon and tragically claimed the lives of nearly 200 individuals [8]. Additionally, over 5000 landslides have occurred in the Three Gorges reservoir area due to a combination of factors, including the region's distinctive geological characteristics, alternating rainy and dry seasons, fluctuations in reservoir levels, and the impact of human construction operations, which directly influenced the social structure and development of the Three Gorges area [9–11].

Landslide susceptibility assessment has garnered significant attention from researchers and specialists in recent years, as it can efficiently provide local geologic disaster manage-

ment departments with reliable and scientifically sound support for implementing essential defense and rescue measures [12–14]. Landslide susceptibility mapping (LSM) draws on an assortment of contributory and predisposing factors to determine the characterization of the geographic arrangement of landslides through either qualitative or quantitative methodologies [15–20]. The approaches to evaluating LSM have continually evolved in response to scientific and technological advancements, yet the landslide susceptibility system remains a fundamental component throughout the entire development process. By comparing the efficiency of supervised machine learning and ensemble learning techniques in LSM, it was revealed that the model-building and forecasting capabilities of boosted regression trees and random forests are slightly superior to flexible discriminant analysis methods [21]. In addition, Boosting, Stacking, and Bagging ensemble learning techniques were coupled with decision tree and artificial neural network methods for LSM. The findings indicate that the application of ensemble learning techniques enhances the accuracy of LSM results [22].

The nature of landslides involves the downward movement of rock and soil along slopes [23]. However, landslide susceptibility assessment has traditionally relied on static factors such as geological and hydrological data, which is obviously not conducive to the recent landslide proneness evaluation [24,25]. Furthermore, the full utilization of deforming landslide characteristics is often unattainable, leading to false negatives and consequently reducing the reliability of landslide susceptibility evaluations. The incorporation of surface deformation data in an appropriate manner can enhance the reliability of the landslide susceptibility results. Conventional terrestrial monitoring stations are characterized by exorbitant costs, implementation difficulties, and limitations in conducting comprehensive macro-monitoring across expansive regions. Interferometric Synthetic Aperture Radar (InSAR) not only addresses the limitations associated with conventional observation sites but also enables continuous and weather-independent monitoring [26,27]. The application of InSAR technology is widely employed across various domains, including urban subsidence, groundwater monitoring, mine detection, and numerous other areas. It has demonstrated the capability to provide high-precision monitoring at the millimeter scale, which is crucial for early warning and prevention of landslide disasters [28–30].

However, the effective integration of InSAR and LSM for landslide susceptibility assessment is still in the exploratory phase, with full consideration of their respective advantages. Fusion techniques based on the Analytic Hierarchy Process method [31] and the Weighted Overlay method [32,33] are constrained by the experts' empirical knowledge, which may introduce uncertainty of results with issues of high subjectivity and a significant risk of false positives [34]. In addition, Kouhartsiouk [35] and Bo et al. [36] used InSAR to update landslide inventory data before conducting landslide susceptibility assessment, which is labor-intensive, time-consuming, and inefficient. And, deformation identified using InSAR does not necessarily indicate the occurrence of a landslide disaster. Building on the aforementioned studies, utilizing various models for evaluating landslide susceptibility and coupling them with InSAR involves more than simply overlaying or visually comparing deformation results with LSM. Instead, it involves a deep integration of them, with a focus on a comprehensive evaluation of the study area. In short, this work seeks to assess and compare the effectiveness of several coupled models in updating LSM using InSAR deformation data and to identify the most optimal landslide dynamic sensitivity evaluation model.

This study involved the construction of five ensemble learning models, including eXtreme Gradient Boosting (XGBoost) [37], Random Forest (RF) [38], Logistic Regression (LR) [39], Gradient Boosting Decision Tree (GBDT) [40], and K-Nearest Neighbor (KNN) [41], to conduct an initial assessment of landslide susceptibility. The Small Baseline Subset-Interferometric Synthetic Aperture Radar (SBAS-InSAR) technology was utilized to determine the ground deformation rate in both the satellite line of sight (LOS) and the vertical direction. Subsequently, the landslide susceptibility evaluation of Shiyan City in Hubei Province was conducted by comparing the impacts of two separate implementations of the

dynamic characteristic factor and the InSAR optimization matrix in order to scientifically incorporate InSAR deformation outcomes with the original landslide susceptibility. The primary objectives encompass delivering precise and reliable scientific support for landslide early warning, rescue, and protective measures in Shiyan City, as well as facilitating the continuation of landslide identification, regional geological hazard investigations, and further academic research.

2. Study Area and Data

2.1. Study Area

This study focuses on Shiyan City, located in the northwestern region of Hubei Province, within the core region of the Qinba Mountain range, along the mid-upper sections of the Han River. The city's topography is characterized by elevated northern and southern regions, while the central area is defined by lower elevations. The landforms in the area are classified into four primary types: hills, low mountains, mid-mountains, and alpine mountains, with mountainous yellow-brown loam being the predominant soil type [42,43]. The predominant geological composition of the mountains consists primarily of limestone and metamorphic rocks, along with extensive fractures, narrower valleys, and drastic height variations. Shiyan City is situated in the north subtropical continent rainy humid climate with an average annual temperature ranging from 13 to 16 °C and an average annual precipitation of 829 mm over the past 20 years. The urban area is characterized by an extensive network of watercourses, with the Blocking River being the most prominent, extending over a length of 338.6 km [44,45]. The official records indicate that the city has experienced a total of 3575 landslides, with 3298 of them having been recorded the type of landslide. There are a total of 204 landslides classified as rocky, 2938 as earthy landslides, and 156 as a combination of rocky and earthy landslides. Figure 1 depicts the geographic location of Shiyan City and the distribution of landslides.

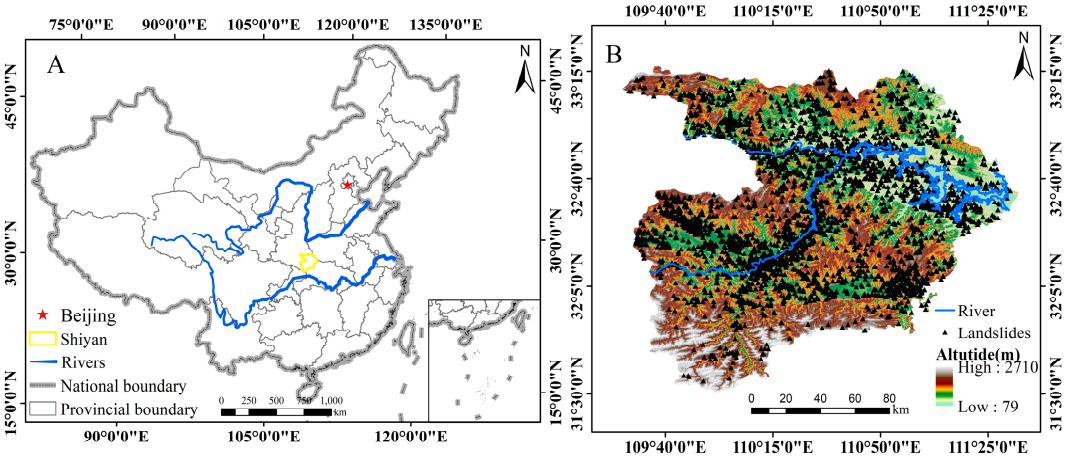

Figure 1. Location of the study area in China. (**A**) map of China, (**B**) map of Shiyan City.

2.2. Data

The study primarily utilizes data from 3529 landslide catastrophe sites—comprising four enormous, seven extra-large, and one hundred eighty-one large landslides—provided by the Natural Resources and Urban Rural Development Bureau of Shiyan City in China. STRM 30 m DEM was employed to determine the topography and hydrological conditions-related landslide impact factors. The national fundamental geographic database, at a scale of 1:250,000, was used for navigating roads and rivers. The indicators of land-use type evaluation were derived from global land cover with a 30 m resolution. The stratigraphy, lithology, and geologic structure were derived from national geologic map data. The Normalized Difference Vegetation Index (NDVI) was computed using four sets of remotely sensed images from Landsat-8 OLI launched by NASA in California, USA 2013, with row and column numbers "125,037", "125,038", "126,037", and "126,038". Sentinel-1A

images from September 2021 to March 2022 were used to generate surface deformation rates. Table 1 tabulates the data sources.

Table 1. Data sources.

Data Type	Data Source	Time
Landslides	http://gtzy.shiyan.gov.cn/ (accessed on 13 March 2023)	2016
Administrative boundaries of Shiyan City	http://datav.aliyun.com/portal/school/atlas/area_selector (accessed on 20 March 2023)	2021
STRM30 m DEM	https://www.gscloud.cn/ (accessed on 20 March 2023)	2009
Land cover	https://www.webmap.cn/commres.do?method=globeIndex (accessed on 5 April 2023)	2010
National basic geographic database	https://www.webmap.cn/commres.do?method=result25W (accessed on 5 April 2023)	2015
National geologic map data	http://www.tuxingis.com/locaspace.html (accessed on 5 April 2023)	2013
Landsat-8 OLI Remote Sensing images	https://www.gscloud.cn/ (accessed on 23 April 2023)	2021
Sentinel-1A images	https://search.asf.alaska.edu/ (accessed on 3 May 2023)	September 2021–March 2022

3. Methods

To effectively address the deficiency of dynamic factors in traditional landslide susceptibility assessment and to enhance the rationality and scientific rigor of LSM in Shiyan City, this study undertakes four core tasks: (1) evaluating landslide susceptibility using multi-models based on static factors; (2) acquiring surface deformation rates; (3) assessing landslide susceptibility by integrating dynamic and static factors; and (4) optimizing the landslide susceptibility assessment using the InSAR optimization matrix. One of the most fundamental aspects is to advance the quantitative analysis techniques of multi-source data and multi-models to achieve the most accurate static landslide susceptibility results. Additionally, it is crucial to process the surface deformation data obtained via SBAS-InSAR and integrate it with the initial landslide susceptibility results. The primary aim of our work is to identify the most effective fusion approach by comparing two methodologies for incorporating InSAR results into landslide susceptibility assessments: the dynamic characteristic factor and the InSAR optimization matrix. Figure 2 depicts the comprehensive technical workflow of the study.

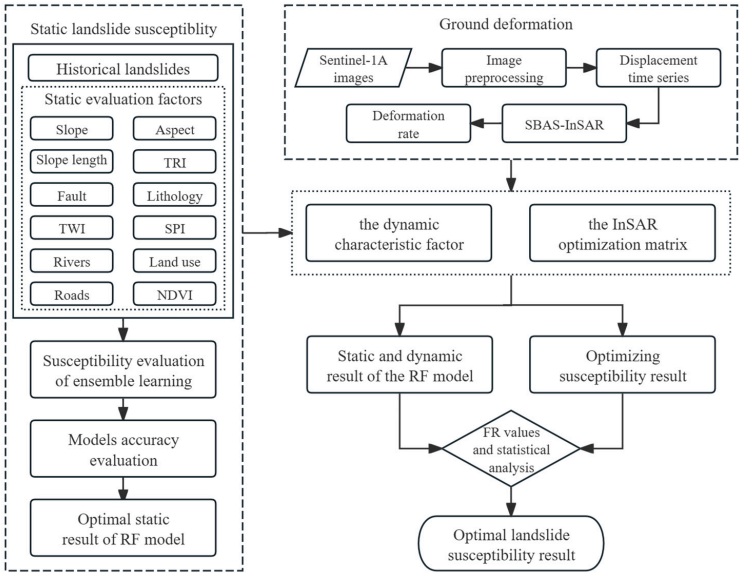

Figure 2. Flowchart of this study.

3.1. Frequency Ratio (FR) Method

The FR approach is a straightforward and widely employed quantitative analysis technique that operates as a single-variable probability analysis method. In geology, it

quantifies the degree of association between the distribution of geologic hazards and disaster-predisposing factors through the calculation of frequency ratios. The magnitude of the FR value is directly proportional to the impact of the environmental factor on the emergence of geohazards; a higher FR value indicates a more significant influence of the environmental factor's interval on the development of geohazards [46,47]. The formula for the FR method is

$$FR = \frac{l_i / L_i}{n_i / N_i} \quad (1)$$

where FR is the frequency ratio, l is the number of landslide rasters in a single environmental factor partition, L is the total number of landslide rasters in the study region, n is the number of rasters in that environmental factor partition, and N is the total number of rasters in the study region.

3.2. SBAS-InSAR Technology Flow

SBAS-InSAR is a ground deformation monitoring technique that processes a series of synthetic aperture radar (SAR) images, akin to the Differential Interferometric Synthetic Aperture Radar (D-InSAR) and the Permanent Scatterer Interferometric Synthetic Aperture Radar (PS-InSAR) techniques [48,49]. In contrast to D-InSAR and PS-InSAR, SBAS-InSAR exhibits greater repeatability, scalability, and precision monitoring results due to the fact that the short spatial-temporal baseline subset combination can suppress the influence of decorrelation caused by random errors. Furthermore, the SBAS-InSAR methodology is capable of handling datasets with varying sample rates, thus enabling a broader spectrum of activities compared to conventional methodologies.

The fundamental principle of SBAS-InSAR involves generating a multi-master image set with temporal and spatial thresholds, modeling and resolving it, and then producing a time series map for the study area. The primary technological procedures are as follows: Initially, the raw data are converted to single look complex images, and further proceedings are conducted with precision orbit ephemerides data. Subsequently, the multi-master image is established for differential interference processing predicated on the temporal and spatial thresholding principles, aimed at reducing the consequences of the atmospheric phase, topographic phase, error phase, and data spatiotemporal correlation. Ultimately, the surface deformation phase of the image set is jointly resolved by means of the least squares approach, and the surface deformation phase is obtained through the singular value decomposition technique, generating deformation results across the entire time series. Figure 3 depicts the Flowchart of SBAS-InSAR.

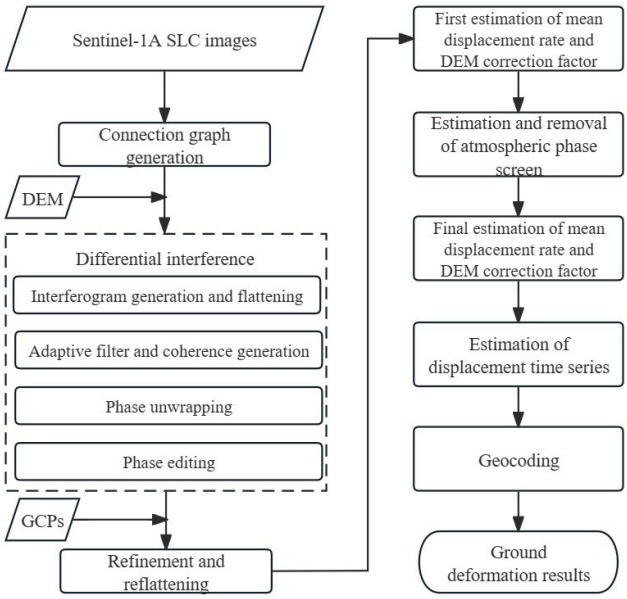

Figure 3. Flowchart of SBAS-InSAR.

To sum up, SBAS-InSAR technology offers significant benefits in terms of repeatability, scalability, and surface morphology capture [50]. The application of this method, which produces precise and detailed data on surface deformation, is increasingly essential in various domains such as ecological conservation, management of natural resources, and urban development [51,52].

3.3. Ensemble Learning Models

Ensemble learning has emerged as a prominent field of study in machine learning, owing to its straightforward premise and exceptional accuracy. It employs a finite set of autonomous learners, referred to as weak learners, to collectively address a given problem. These weak learners are then combined to form a composite model, known as strong learners. The performance of the strong learners is contingent upon the output of each individual learner within the ensemble, thereby enabling a unified solution to the problem at hand. Current ensemble learning methodologies can be broadly categorized into two primary classes, depending on the generation of individual learners.

1. Boosting: The sequential serialization method is necessary due to the interdependencies between individual learners, both in terms of backward and forward progression.
2. Bagging: The parallelization approach is developed simultaneously as a result of the relative independence among individual learners.

Figure 4 illustrates the core principles of ensemble learning, which is implemented through a two-part process: the learning phase and the application phase.

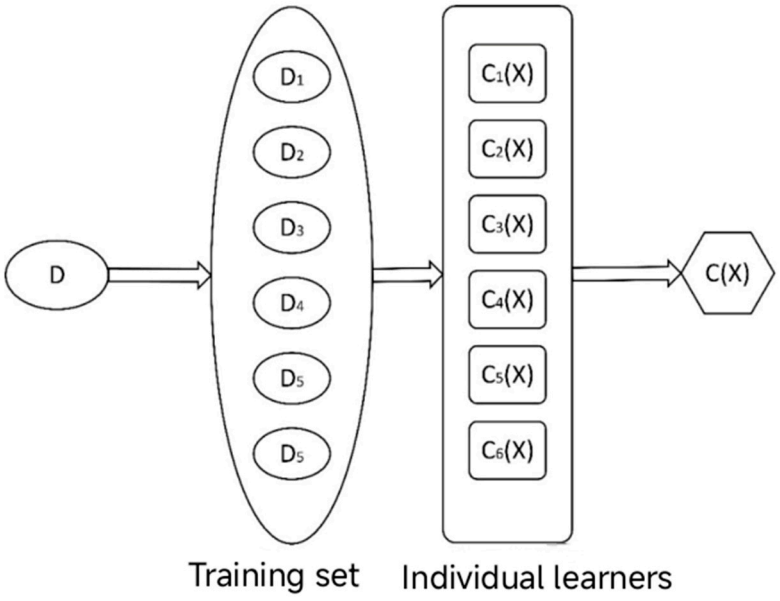

Figure 4. Principles of ensemble learning.

Learning phase: Using some methods to make the training set D produce T subsets, such as $D_1, D_2, \ldots, D_T$, and defining a single classifier (base classifier) for each subset, such as $C_1, C_2, \ldots, C_T$, thus integrating the system $C(x) = \{ C_1, C_2, \ldots, C_T\}$.

Application phase: For the input samples $x = (x_1, x_2, \ldots, x_p)$, each base classifier C_t ($1 \leq t \leq T$) can output its own judgment $C_t(x)$. The ultimate classification outcome is determined by combining the results of all the basic classifiers, typically by methods like weighted summation or majority vote.

Given the exceptional performance of ensemble learning in processing complex data with high precision, generalization, and robustness, we selected five widely used ensemble learning models, namely XGBoost, RF, LR, GBDT, and KNN, for landslide sensitivity assessment. Among these models, GBDT integrates the results of multiple decision trees, capturing the nonlinear relationship between evaluation factors and effectively handling

complex multi-source data. XGBoost enhances training and prediction efficiency through algorithm optimization and parallel processing, performing well on large datasets. RF can assess the feature importance of evaluation factors to identify the key influencing factors and demonstrate robustness against overfitting. LR is suitable for analyzing and modeling the potential linear relationships in landslide susceptibility assessment. KNN, an adaptable method that utilizes nearest-neighbor characteristics, is particularly effective for local area evaluation.

4. Results

4.1. Landslide Causative Static Factors

The geological environment significantly influences the likelihood of landslide hazards. Incorporating the fundamental principles of geologic catastrophe development in Shiyan City, twelve static evaluation factors were preliminarily identified, including four topographic and geomorphologic factors (terrain roughness index (TRI), aspect, slope length, and slope), two geologic and lithologic factors (distance from fault and lithology), three hydrologic factors (topographic wetness index (TWI), stream power index (SPI), and distance from rivers), and three land cover factors (land use, distance from roads, and NDVI). After format conversion, discretization, spatial analysis, and other relevant procedures, each evaluation index is resampled into a raster with a 30 m resolution, which is then utilized to determine the evaluation units. The continuous variables, such as slope, slope length, etc., were split under five classifications by the natural breakpoint method, and the multi-value extraction to point tool was employed to generate the assessment dataset. To address the imbalance between landslide and non-landslide points, samples were allocated in a 1:2 ratio for each category, with 30% designated as the test set and 70% as the training set, ensuring sample balance and training model accuracy. By employing five ensemble learning models—XGBoost, RF, LR, GBDT, and KNN—along with accuracy assessment and comparative statistical analysis, the most effective results were achieved in the assessment of static landslide susceptibility. Figure 5 and Table 2 illustrate information of causative static factors.

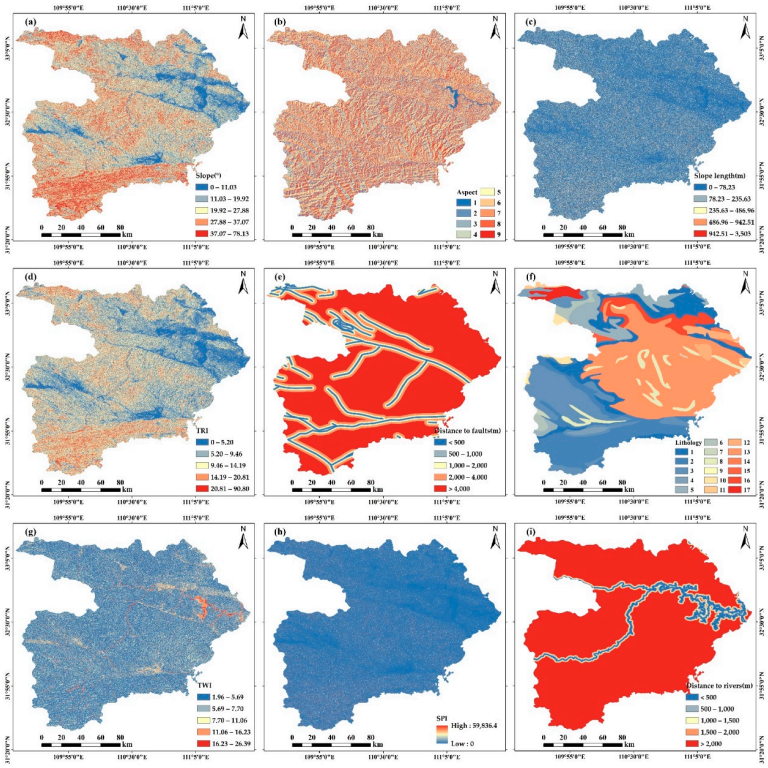

Figure 5. *Cont.*

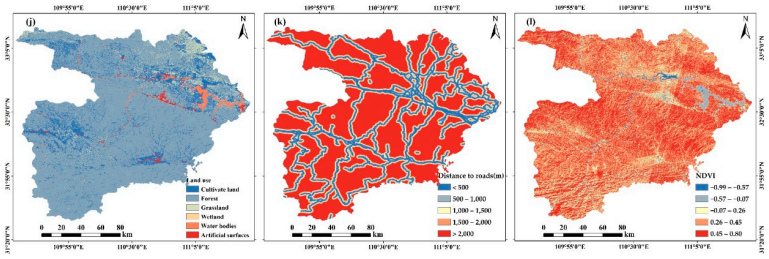

Figure 5. Twelve static evaluation factors: (**a**) slope; (**b**) aspect; (**c**) slope length; (**d**) TRI; (**e**) distance from fault; (**f**) lithology; (**g**) TWI; (**h**) SPI; (**i**) distance from rivers; (**j**) land use; (**k**) distance from roads; (**l**) NDVI. The aspect groups are described as follows: 1: flatness; 2: north; 3: northeast; 4: east; 5: southeast; 6: south; 7: southwest; 8: west; 9: northwest. The lithology groups are described as follows: 1: PT1; 2: EO; 3: S1; 4: C1; 5: E; 6: O; 7: OPZ; 8: VPT3; 9: HUI; 10: GREEN; 11: C2P; 12: K2; 13: PT3; 14: EE; 15: BLUE; 16: PT2; 17: D.

Table 2. Values for parts of causative factors.

Factors	Class	Landslides	Frequency of Landslides	Classification Value
Slope (°)	0–11.03	556	15.81%	1
	11.03–19.92	1398	39.75%	2
	19.92–27.88	1084	30.82%	3
	27.88–37.07	390	11.09%	4
	37.17–78.13	89	2.53%	5
Slope lenth (m)	0–78.23	2225	63.26%	1
	78.23–235.63	839	23.86%	2
	235.63–486.96	335	9.53%	3
	486.96–942.51	106	3.01%	4
	942.51–3503	12	0.34%	5
TRI	0–5.20	1081	30.74%	1
	5.20–9.46	1570	44.64%	2
	9.46–14.19	645	18.34%	3
	14.19–20.81	196	5.57%	4
	20.81–90.80	25	0.71%	5
Distance to faults (m)	<500	213	6.06%	1
	500–1000	182	5.17%	2
	1000–2000	358	10.18%	3
	2000–4000	626	17.80%	4
	>4000	2138	60.79%	5
TWI	1.96–5.69	1335	37.96%	1
	5.69–7.70	1727	49.10%	2
	7.70–11.06	336	9.55%	3
	11.06–16.23	97	2.76%	4
	16.23–26.39	22	0.63%	5
SPI	0–934	3452	98.15%	1
	934–4207	61	1.73%	2
	4207–10,284	4	0.11%	3
	10,284–22,905	0	0.00%	4
	22,905–59,836	0	0.00%	5
Distance to rivers (m)	<500	306	8.70%	1
	500–1000	229	6.51%	2
	1000–1500	161	4.58%	3
	1500–2000	118	3.36%	4
	>2000	2703	76.86%	5
Land use	Cultivate land	1657	47.11%	1
	Forest	1532	43.56%	2
	Grassland	267	7.59%	3
	Wetland	0	0.00%	4
	Water bodies	10	0.28%	5
	Artificial surfaces	51	1.45%	6

Table 2. *Cont.*

Factors	Class	Landslides	Frequency of Landslides	Classification Value
Distance to roads (m)	<500	1045	29.71%	1
	500–1000	360	10.24%	2
	1000–1500	307	8.73%	3
	1500–2000	300	8.53%	4
	>2000	1505	42.79%	5
NDVI	−0.99–−0.57	10	0.28%	1
	−0.57–−0.07	65	1.85%	2
	−0.07–0.26	759	21.58%	3
	0.26–0.45	1609	45.75%	4
	0.45–0.80	1074	30.54%	5

4.2. Static Factors Evaluation Results

The outcomes obtained from the five assessment models for landslide susceptibility span a numerical range spanning from zero to one. These data were reclassified into five distinct categories, namely very low, low, moderate, high, and very high zones, utilizing the natural breakpoint method. The predictive performance of the models was assessed through the receiver operator characteristic (ROC) curve, which assesses prediction accuracy based on the area under the curve (AUC), thereby quantifying computational precision. Figure 6 depicts the static factors evaluation results and the ROC curves of different models.

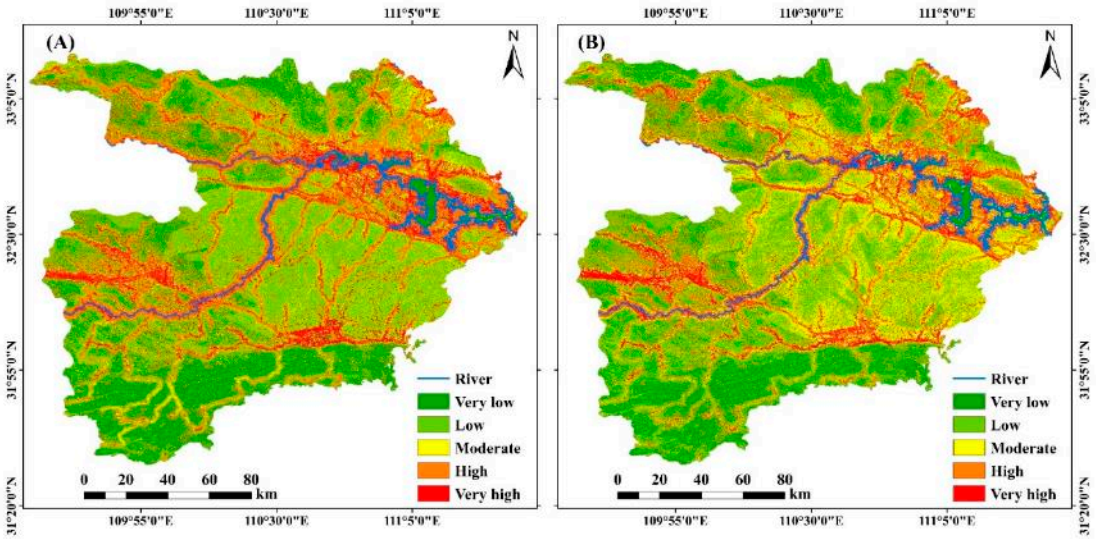

Figure 6. *Cont.*

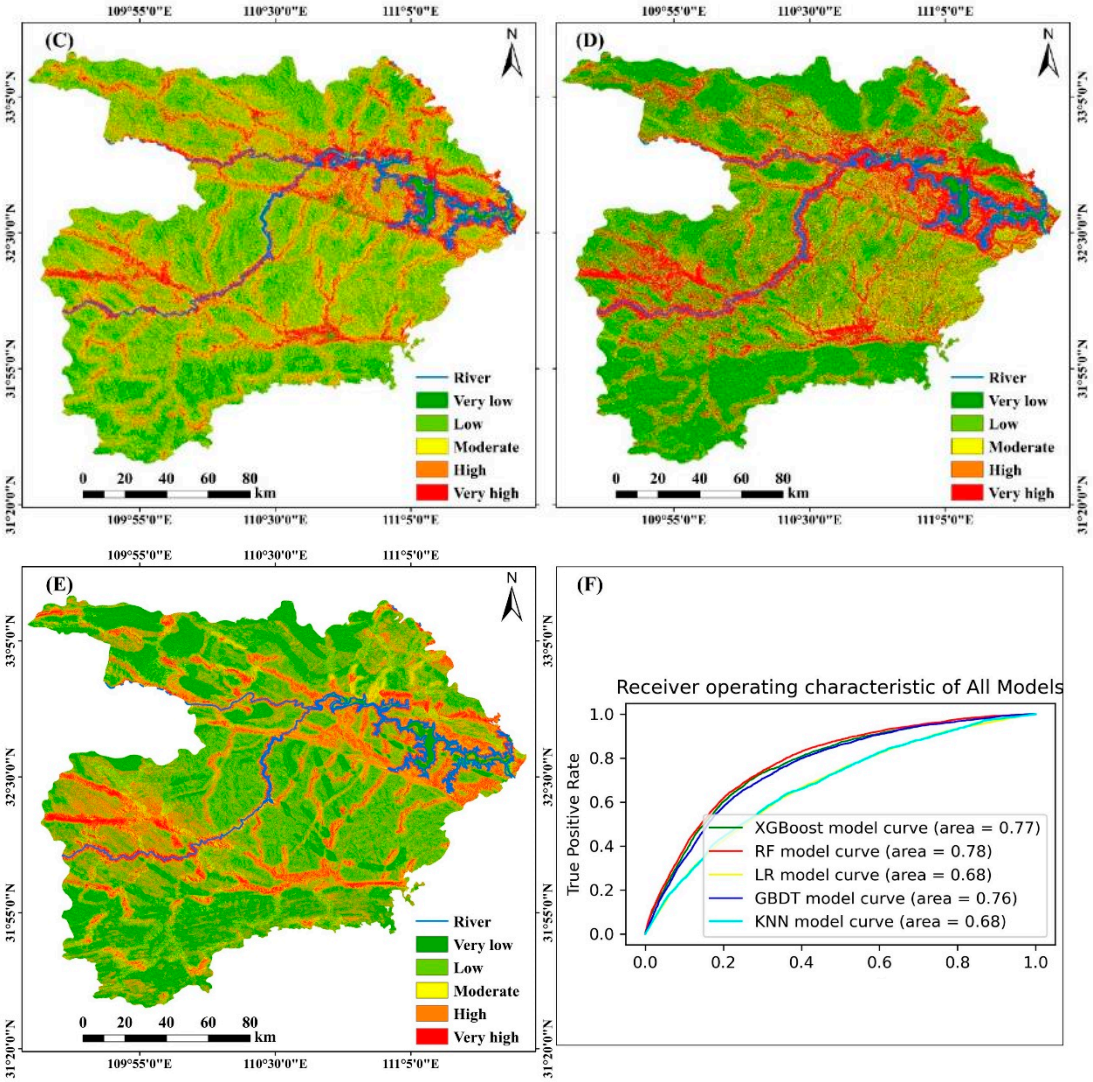

Figure 6. Landslide susceptibility maps. (**A**) map of XGBoost model, (**B**) map of RF model, (**C**) map of LR model, (**D**) map of GBDT model, (**E**) map of KNN model, and (**F**) map of ROC curves by different models.

The ROC accuracy of each model, GBDT, XGBoost, and RF, illustrates greater reliability, with model AUC values exceeding 0.75. To further identify the optimal model results, this work quantifies the number of rasters, the number of landslides, and the percentage within each susceptible interval. The findings are presented in Table 3.

Table 3. Landslide susceptibility level zoning.

Model	Landslide Susceptibility Level	Number of Pixels in Domain	Percent of Domain (%)	Number of Landslides	Percent of Landslides (%)
GBDT	Very low	10,880,445	40.98	336	9.57
	Low	4,985,541	18.78	365	10.40
	Moderate	3,362,087	12.66	423	12.05
	High	2,626,950	9.89	502	14.30
	Very high	4,692,903	17.68	1884	53.68
LR	Very low	4,728,064	17.80	216	6.15
	Low	9,888,848	37.25	765	21.79
	Moderate	4,700,527	17.71	605	17.24
	High	4,751,518	17.90	1005	28.63
	Very high	2,478,969	9.34	919	26.18

Table 3. *Cont.*

Model	Landslide Susceptibility Level	Number of Pixels in Domain	Percent of Domain (%)	Number of Landslides	Percent of Landslides (%)
RF	Very low	4,701,470	17.71	65	1.85
	Low	9,470,206	35.67	399	11.37
	Moderate	6,025,650	22.70	697	19.86
	High	3,801,322	14.31	1032	29.40
	Very high	2,549,278	9.60	1317	37.52
XGBoost	Very low	5,481,662	20.64	86	2.45
	Low	9,441,984	35.57	498	14.19
	Moderate	3,442,159	12.97	336	9.57
	High	5,503,552	20.73	1292	36.81
	Very high	2,678,569	10.90	1298	36.98
KNN	Very low	9,693,047	36.51	529	15.07
	Low	6,904,034	26.01	712	20.28
	Moderate	2,712,572	10.21	412	11.73
	High	5,350,227	20.15	1165	33.19
	Very high	1,888,046	7.11	692	19.71

The landslide susceptibility result of the RF model exhibits superior ROC precision. The high and very high susceptibility zones encompass more landslide hazard sites within a smaller area. The regions of high susceptibility are primarily located along rivers and in certain lowland areas, aligning with the fundamental principles of geologic hazards formation. Consequently, it is evident that the RF model is more effective in assessing outcomes, and the LSM result derived from the static factors using the RF model is designated as A.

4.3. SBAS-InSAR Results

Geological hazards such as landslides, collapses, and ground subsidence have consistently posed a significant threat to social security and economic development in Shiyan City. These potential hazards are typically accompanied by notable surface deformation [53,54]. This study utilized the ENVI SARscape 5.6.2 radar image processing software, developed by Sarmap, to apply the SBAS-InSAR methodology for identifying areas of surface deformation in Shiyan City for ascending orbiting Sentinel-1A images from September 2021 to March 2022. The surface deformation information acquired through the SBAS-InSAR technique can be leveraged for early detection, monitoring, and risk assessment of geological hazards, thereby providing essential data support for local territorial spatial planning [55]. The SAR dataset consists of interferometric pairs of radar images with small spatial baselines and short temporal intervals, determined through the time series analysis technique to monitor regional deformation. The interferometric deformation results of the SAR dataset are subsequently resolved using differential interferometry to extract surface deformation in both the vertical and the LOS directions. Figure 7 depicts the deformation rate obtained by the SBAS-InSAR technique. The deformation rate along the LOS direction ranges from −68.7518 mm/year to 39.4417 mm/year, while the vertical deformation rate ranges from −82.7976 mm/year to 47.4995 mm/year.

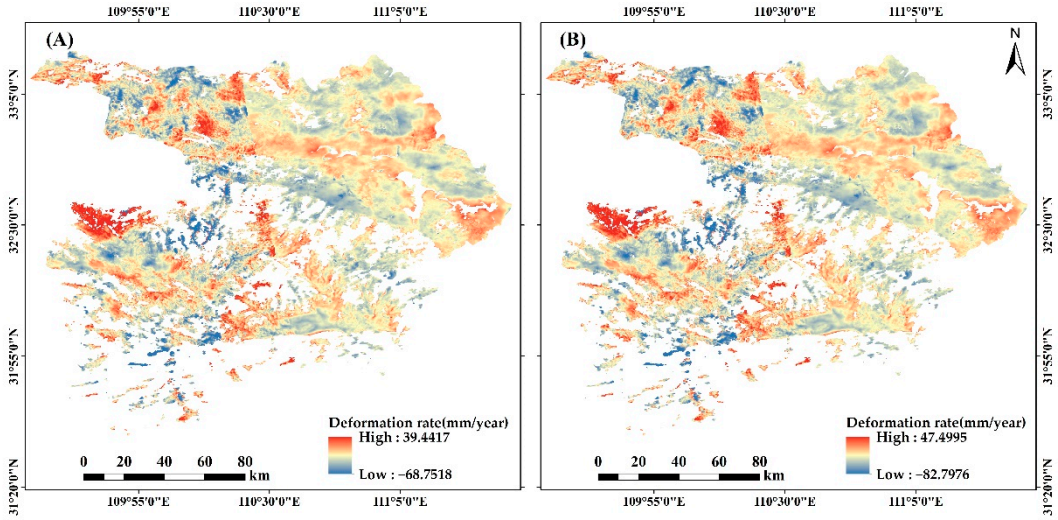

Figure 7. Deformation rate. (**A**) map of deformation rate in the LOS direction, (**B**) map of deformation rate in the vertical direction.

4.4. Evaluation of Combined Dynamic and Static Factors

The landslides move downward, and the positive value of the surface deformation in the vertical direction indicates upward movement, while the negative value signifies downward movement. In light of the aforementioned principles, the positive portion of the vertical surface deformation rate is adjusted to 0, preserving only the negative values. In accordance with the surface deformation rate distribution map, the vast majority of the study area exhibits a deformation rate between 0 and 5.844 mm/year, with high rates of deformation sporadically distributed. Subsequently, by classifying the screened vertical deformation rates as five sections, the dynamic characteristic factor is integrated with the static evaluation factors, forming a new dataset. This dataset, comprising 13 dynamic and static evaluation factors overall, is then input into the optimal evaluation RF model in Section 4.2 to generate the landslide susceptibility evaluation result B. Figure 8 depicts the dynamic characteristic factor and the evaluation result of combined static and dynamic factors.

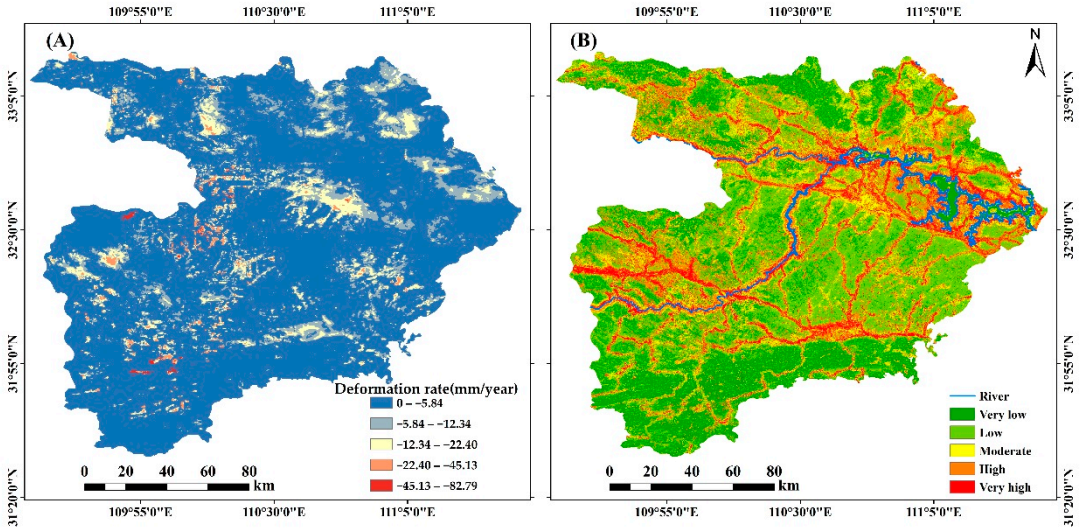

Figure 8. (**A**) map of the dynamic characteristic factor; (**B**) map of static and dynamic factors landslide susceptibility result of the RF model.

4.5. InSAR Optimization Matrix Result

The positive values of the surface deformation rate in the LOS direction indicate the proximity to the flight direction, while the negative values indicate the distance from the satellite's flight direction. In this study, the absolute deformation rate in the LOS direction is categorized into five distinct groups: V1 (0–10 mm/year), V2 (10–20 mm/year), V3 (20–30 mm/year), V4 (30–40 mm/year), and V5 (>40 mm/year). Similarly, the static factor LSM result from the RF model, denoted as result A, is also classified into five groups: H1 (very low), H2 (low), H3 (moderate), H4 (high), and H5 (very high). The generation of the landslide susceptibility optimization matrix involves the combination of the above two factors, as illustrated in Table 4. And Figure 9 depicts the absolute value of deformation rate in the LOS direction and the optimizing landslide susceptibility result.

Table 4. InSAR optimization matrix.

	V1	V2	V3	V4	V5
H1	1	2	3	4	5
H2	2	2	3	4	5
H3	3	3	3	4	5
H4	4	4	4	4	5
H5	5	5	5	5	5

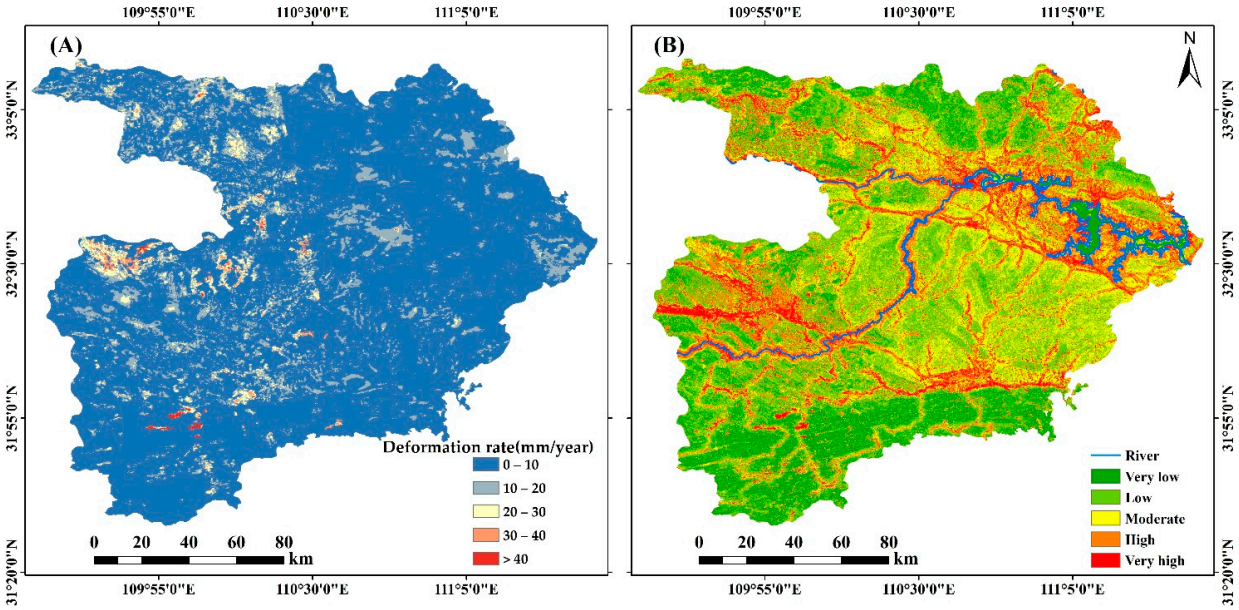

Figure 9. (**A**) map of absolute value of deformation rate in the LOS direction, (**B**) map of optimizing susceptibility result.

5. Discussion

5.1. Analysis of Research Results

Landslide susceptibility assessment has traditionally relied heavily on static data (e.g., topography, hydrology) for decades, while landslides are intended to be the dynamic nature associated with the movement of rock and soil along a sloped surface, which is influenced by rainfall, earthquakes, and man-made cuts in slopes and downslope slides, either as a whole or in scattered pieces [23], under the influence of gravity. The lack of dynamic data, such as surface deformation, makes it challenging to comprehensively analyze the characteristics of deforming landslides [6,49,56], leading to false-positive or false-negative landslide susceptibility results and undermining the reliability of LSM.

Advances in remote sensing technology, however, have significantly enhanced both the sources and efficiency of data collection, enabling more accurate landslide susceptibility assessments [57].

In recent years, InSAR technology has gained significant traction among geohazard practitioners and researchers, driven by the availability of open access to Sentinel-1A remote sensing image data, which has exhibited excellent applicability in the early identification of potential landslides and the monitoring of deformation signs. Moreover, previous studies have shown that coupling InSAR technology with geological theories could enhance the sensitivity of landslide threat assessments to some extent [58]. Despite these advancements, the effective utilization of the surface deformation information gathered through InSAR technology for LSM remains an area of active research and development. With the primary objective of landslide susceptibility evaluation in Shiyan City, two extensively used approaches for integrating InSAR deformation findings with landslide susceptibility results were selected in this research: the dynamic characteristic factor and the InSAR optimization matrix. The magnitude of the FR value can serve as an indicator of the significance of the interval in which the environmental elements are situated in the formation of geohazards. This study conducts a statistical analysis of the FR values obtained from two distinct InAR fusion landslide susceptibility assessments, and higher FR values correspond to a greater number of landslide rasters per unit area, hence indicating a more accurate evaluation.

The susceptibility ranges classified as high and very high are closely aligned in terms of both the proportion of rasters and the percentage of landslides, in accordance with the statistical results in Table 5. There is a slight differentiation between the intervals of the very low and low susceptibility classes, while a significant disparity is observed among the moderate susceptibility classes. For the high susceptibility class interval, the result of the dynamic characteristic factor is slightly lower than that of the InSAR optimization matrix, with a difference of less than 0.02 in FR values. Conversely, for the remaining four intervals, the dynamic characteristic factor is higher. Overall, the dynamic characteristic factor yields a higher FR value, indicating a greater number of landslide rasters per unit area per susceptibility partition and superior predictive performance.

Table 5. Comparison between different evaluation approaches.

Evaluation Approach	Landslide Susceptibility Level	Number of Pixels in Domain	Percent of Domain (%)	Number of Landslides	Percent of Landslides (%)	FR
dynamic characteristic factor	Very low	6,146,899	23.15	99	2.82	0.12
	Low	9,775,531	36.82	505	14.39	0.39
	Moderate	3,985,362	15.01	481	13.70	0.91
	High	4,036,548	15.20	1063	30.28	1.99
	Very high	2,603,586	9.80	1362	38.80	3.96
InSAR optimization matrix	Very low	4,235,667	15.95	47	1.3	0.08
	Low	9,443,633	35.57	382	10.88	0.3
	Moderate	6,344,038	23.90	713	20.31	0.85
	High	3,942,904	14.85	1048	29.86	2.01
	Very high	2,581,684	9.72	1320	37.61	3.87

Figure 6 illustrates that the regions with high and very high susceptibility are primarily concentrated around the confluence of Zhuxi County and Zhushan County, Fang County Center, Zhangwan District, Xunyang District, Maohuai District, and the junction of Danjiangkou City alongside the Han River. Table 6 displays the statistical data related to the evaluation of the dynamic characteristic factor. The rate of hazard development per 100 square kilometers and the density of landslides progressively increase as the susceptibility level rises. In the zone characterized by very high susceptibility, the landslide density reaches 0.58, with landslide hazards developing over an area of 6.30 km^2.

Table 6. Landslide susceptibility result statistics incorporating dynamic characteristic factor.

Landslide Susceptibility Level	Zoning Area (km^2)	Number of Landslides	Landslides Density	Landslides Area (km^2)	Percentage of Landslides/100 km^2
Very low	5532.21	99	0.02	3.48	0.06
Low	8797.98	505	0.06	18.72	0.21
Moderate	3586.83	481	0.13	17.81	0.50
High	3632.89	1063	0.29	46.08	1.27
Very high	2343.23	1362	0.58	147.63	6.30

5.2. Effect Analysis of SBAS-InSAR Results

Using SBAS-InSAR technology to obtain deformation information, the surface deformation rate predominantly ranges from 0 to 10 mm/y in the vertical direction as well as the LOS direction. The regions with significant deformation exhibit a scattered, point-like distribution. The InSAR optimization matrix, determined by expert experience, primarily addresses false negatives when correcting landslide susceptibility results. Consequently, small areas with a low landslide susceptibility rating and a major concentration of deformation are directly classified as high or very high susceptibility zones owing to the optimization matrix, thereby highlighting a notable limitation.

Gini importance was measured by calculating the average reduction in the Gini index across all decision tree nodes for each feature in the RF model [59], and the importance scores of each factor were ranked to ascertain the contribution value to the landslide susceptibility results. The final characteristic importance of each factor is displayed in Figures 10 and 11. Notably, some topographic and hydrological factors exhibit minimal impact. Conversely, the distance from rivers and roads exerts the greatest influence, while the vertical deformation rate is ranked fourth. This indicates that the RF model effectively incorporates surface deformation results.

Two regions with large deformation, labeled A and B, were selected to compare the static factors evaluation results, the combined dynamic and static factors evaluation results, and the InSAR optimization matrix results in order to further identify the optimal method to optimize landslide susceptibility outcomes. Figure 12 reveals that the susceptibility rating of the InSAR optimization matrix results significantly increases when the deformation is more concentrated in regions A and B, leading to over-correcting false negatives. In contrast, the combined dynamic and static factors evaluation results comprehensively consider surface deformation data and effectively incorporate geological circumstances to accurately adjust the static landslide susceptibility outcomes. Overall, combining dynamic and static factors in landslide susceptibility assessment allows for a more comprehensive exploration of the spatial distribution of landslides, providing more dependable recommendations for early warning of landslide disasters.

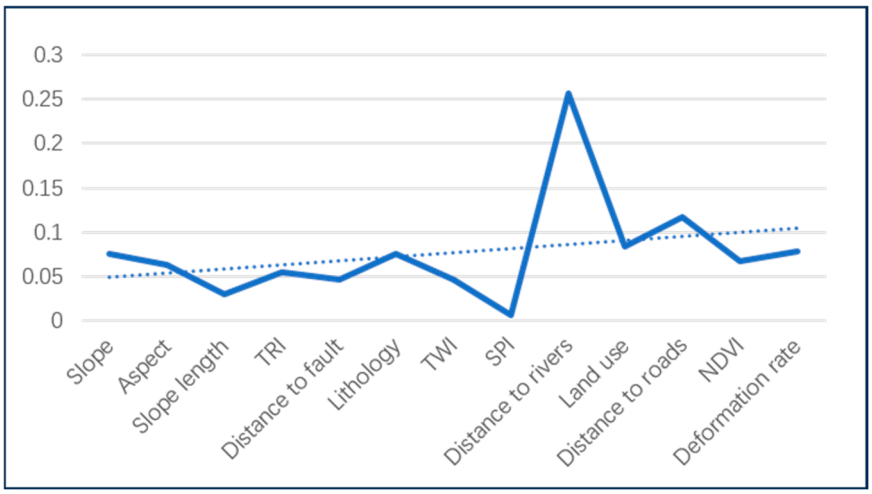

Figure 10. The importance value of factors in the RF model.

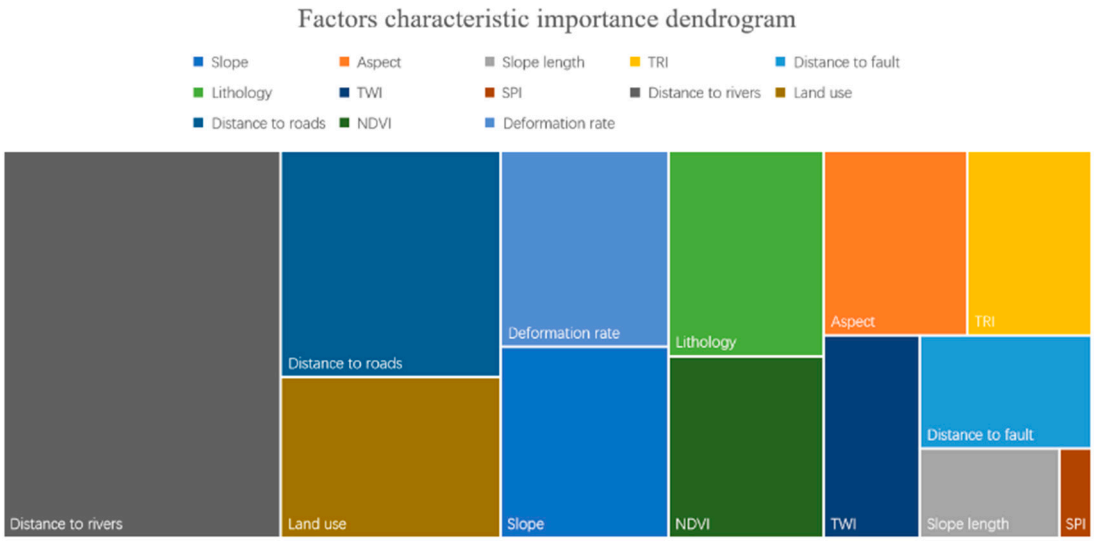

Figure 11. The dendrogram of each factor's characteristic importance in the RF model.

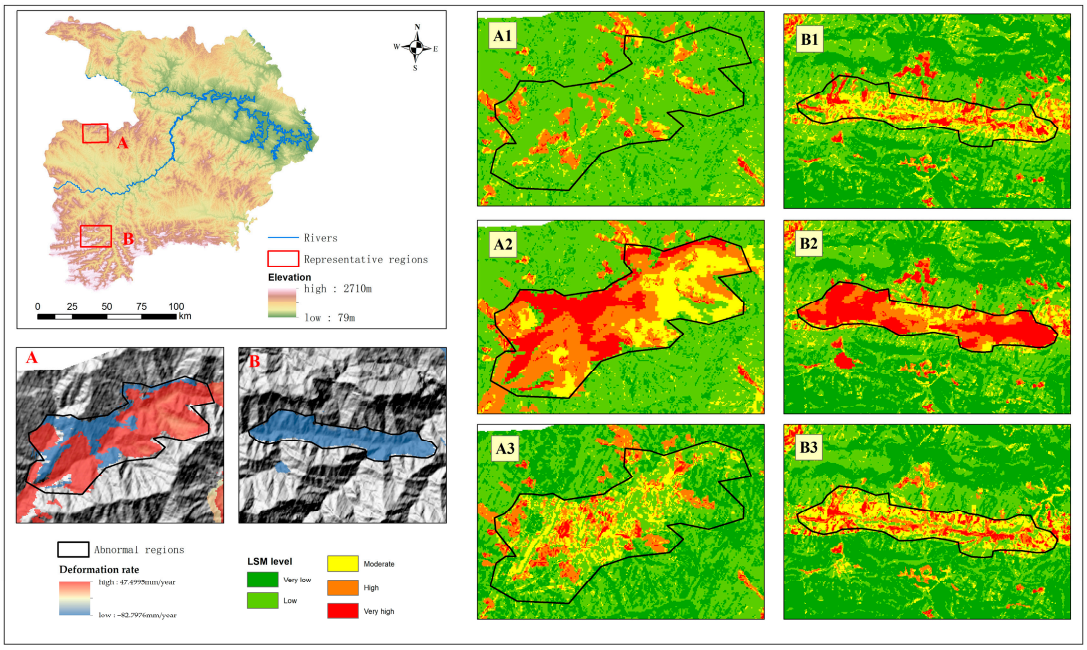

Figure 12. Typical regional comparisons. (**A**,**B**) represent two typical regions with large deformation; (**A1**,**B1**) represent static factors evaluation results; (**A2**,**B2**) represent InSAR optimization matrix results; (**A3**,**B3**) represent evaluation results of combined dynamic and static factors.

5.3. Landslide Disaster Prevention and Control Recommendations

The Yaotan River landslide series is located within the geographical boundaries of Jiahe Town, Xunxi County, Shiyan City, and belongs to the Han River Basin. The geographic coordinates are east longitude 110°00′19″ and north latitude 32°53′46″. This area is characterized by the schist precipitation, reservoir seepage, creep-slip type of landslides, without the presence of weir lakes. The survey identified 17 landslides of numerous shapes within the region, distributed from west to east in four landslide groups, namely Qiaogou, Jiehe-Xinmiao-Shihuiyao, Yaotan River-No. 2 school in town, and Tankou-Xiaowanggou. Among them, the Qiaogou group includes four landslides such as Qiao1 to Qiao4; the Jiehe-Xinmiao-Shihuiyao group contains Xin1 landslide; the Yaotan river-No. 2 school in town group includes four landslides such as Yao1, Yao2, Yao3, and Yao middle school; Tankou-Xiaowanggou is distributed with eight landslides such as Tan1 to Tan 8. The

landslide series is characterized by a cumulative volume of 13,590,000 cubic meters, an aggregate area of 950,000 square meters, and an average thickness of 14 m, impacting around 1500 individuals. It constitutes an unstable situation, amounting to a projected revenue loss of 50 million yuan and posing a significant risk.

The manifestation of the deformation of the Yaotan River landslides series is evident through various phenomena, such as pulling apart house walls, tilting and collapsing of houses, slipping of house foundations, twisting of cultivated land and roads, collapsing of bastion walls, and cracks in the ground. The evident characteristics of horizontal shear displacement can be observed at the leading edge of the landslide. The collapse of rock and soil bodies, landslides, and subsidence frequently occur along highways during or following periods of intense or prolonged rainfall. These events are typically accompanied by the appearance of ground fissures, small drum mounds, and small dislocated bodies. The Yaotan River landslide series has been classified as possessing diminished potential energy as a result of the geotechnical characteristics of the accumulation layer, hydrodynamic circumstances, and analysis of deformation. Traction and push-type creep slip are the primary deformation forms.

The Yaotan River landslide series is situated in the mountainous region of Northwest Hubei, where the key factor contributing to the risk of landslides is the region's geologically inferior environment. The extensive magnitude and the loose composition of its materials pose significant risks to both the implementation of the South-to-North Water Diversion Project and the security of the Danjiangkou Reservoir located downstream along the Han River.

In recent years, landslides have occurred with increasing frequency due to the combined effects of unfavorable elements involving rainfall and human engineering activity. These events have had severe social and economic impacts, prompting local governments to allocate significant resources for disaster mitigation. The presence of landslides has become a significant impediment to the growth and progress of the local economy. Specifically considering the environmental context of the Yaotan River landslide series, the Xin 1 landslide is believed to present significant hazards with the potential for catastrophic consequences. To mitigate the potential for further displacement of the Xin 1 landslide body, it is recommended to implement cut-square load reduction measures and construct support and blocking structures. Furthermore, the removal and diversion of the landslide debris both upstream and downstream of the Hanjiang River are essential to reduce stress exerted on the river banks, enhance the stability of the landslide areas, and, if necessary, facilitate the relocation of affected residents to alternative shelters. Surface drainage facilities should be constructed near the Yaotan River-No. 2 school in town group to prevent water infiltration, alleviate groundwater pressure, and avoid erosion of potential landslide surfaces. For the Tankou-Xiaowanggou group, it is crucial to install drainage systems to improve soil stability and reduce the force of landslides. Environmental protection measures, such as enhancing vegetation, are vital to prevent slope instability and surface erosion, thereby reducing landslide occurrences. The Qiaogou landslide group poses a relatively moderate danger; hence, it is advisable to implement the practice of converting cropland into wood as a means of preventing soil erosion and soil rock desertification.

6. Conclusions

A preliminary landslide susceptibility assessment was conducted using the RF model, which is known for its proficiency in handling extensive datasets and complex feature connections, as well as its robustness against overfitting. Aiming at the problem that traditional landslide susceptibility assessment lacks dynamic factors and struggles to capture deformation characteristics, this paper introduces SBAS-InSAR to extract surface deformation information. Subsequently, two methods of incorporating the InSAR results into landslide susceptibility assessment are explored, and their respective advantages and disadvantages are analyzed. The findings demonstrate that it is more meaningful to incorporate InSAR results into landslide susceptibility assessment as a dynamic factor.

Nevertheless, further improvements are necessary in subsequent studies due to data accessibility issues, inherent constraints of InSAR technology, and the complexity of landslide hazard occurrence. Based on the current research findings, further extensive research can be carried out, focusing on the early identification of landslides and the implementation of an early warning system for landslides.

Author Contributions: Conceptualization, X.W. and J.W.; methodology, X.Q.; software, B.P.; formal analysis, X.W. and X.Q.; data curation, X.Q. and J.W.; writing—original draft preparation, X.Q. and B.P.; writing—review and editing, X.W., J.W.and X.Q.; project administration, X.W. and B.P. All authors have read and agreed to the published version of the manuscript.

Funding: This research was funded by [the National Natural Science Foundation of China] grant number [42071429] and [the Open Fund of Key Laboratory of Urban Land Resources Monitoring and Simulation, Ministry of Natural Resources] grant number [KF-2023-08-19].

Data Availability Statement: The data supporting the findings of this study are available from the corresponding author upon reasonable request.

Conflicts of Interest: The authors declare no conflicts of interests.

References

1. Confuorto, P.; Di Martire, D.; Infante, D.; Novellino, A.; Papa, R.; Calcaterra, D.; Ramondini, M. Monitoring of remedial works performance on landslide-affected areas through ground-and satellite-based techniques. *Catena* **2019**, *178*, 77–89. [CrossRef]
2. Perera, E.N.C.; Jayawardana, D.T.; Jayasinghe, P.; Bandara, R.M.S.; Alahakoon, N. Direct impacts of landslides on socio-economic systems: A case study from Aranayake, Sri Lanka. *Geoenviron. Disasters* **2018**, *5*, 11. [CrossRef]
3. Zhou, X.; Wen, H.; Zhang, Y.; Xu, J.; Zhang, W. Landslide susceptibility mapping using hybrid random forest with GeoDetector and RFE for factor optimization. *Geosci. Front.* **2021**, *12*, 101211. [CrossRef]
4. Dai, K.; Li, Z.; Xu, Q.; Burgmann, R.; Milledge, D.G.; Tomas, R.; Fan, X.; Zhao, C.; Liu, X.; Peng, J.; et al. Entering the era of earth observation-based landslide warning systems: A novel and exciting framework. *IEEE Geosci. Remote Sens. Mag.* **2020**, *8*, 136–153. [CrossRef]
5. Fang, K.; Tang, H.; Li, C.; Su, X.; An, P.; Sun, S. Centrifuge modelling of landslides and landslide hazard mitigation: A review. *Geosci. Front.* **2023**, *14*, 101493. [CrossRef]
6. Zhou, C.; Cao, Y.; Hu, X.; Yin, K.; Wang, Y. Enhanced dynamic landslide hazard mapping using MT-InSAR method in the Three Gorges Reservoir Area. *Landslides* **2022**, *19*, 1585–1597. [CrossRef]
7. Vargas-Cuervo, G.; Hernández-Peña, Y.T.; Zafra-Mejía, C.A. Challenges for Sustainable Urban Planning: A Spatiotemporal Analysis of Complex Landslide Risk in a Latin American Megacity. *Sustainability* **2024**, *16*, 3133. [CrossRef]
8. Bommer, J.; Ledbetter, S. The San Salvador earthquake of 10th October 1986. *Disasters* **1987**, *11*, 83–95. [CrossRef]
9. Cao, Y.; Yin, K.; Zhou, C.; Ahmed, B. Establishment of landslide groundwater level prediction model based on GA-SVM and influencing factor analysis. *Sensors* **2020**, *20*, 845. [CrossRef]
10. Tang, H.; Wasowski, J.; Juang, C.H. Geohazards in the three Gorges Reservoir Area, China–Lessons learned from decades of research. *Eng. Geol.* **2019**, *261*, 105267. [CrossRef]
11. Zhang, Y.; Zhang, Z.; Xue, S.; Wang, R.; Xiao, M. Stability analysis of a typical landslide mass in the Three Gorges Reservoir under varying reservoir water levels. *Environ. Earth Sci.* **2020**, *79*, 42. [CrossRef]
12. Cantarino, I.; Carrion, M.A.; Goerlich, F.; Ibañez, V.M. A ROC analysis-based classification method for landslide susceptibility maps. *Landslides* **2019**, *16*, 265–282. [CrossRef]
13. Merghadi, A.; Yunus, A.P.; Dou, J.; Whiteley, J.; ThaiPham, B.; Bui, D.T.; Avtar, R.; Abderrahmane, B. Machine learning methods for landslide susceptibility studies: A comparative overview of algorithm performance. *Earth-Sci. Rev.* **2020**, *207*, 103225. [CrossRef]
14. Zhao, Z.; He, Y.; Yao, S.; Yang, W.; Wang, W.; Zhang, L.; Sun, Q. A comparative study of different neural network models for landslide susceptibility mapping. *Adv. Space Res.* **2022**, *70*, 383–401. [CrossRef]
15. Chen, T.; Zhu, L.; Niu, R.-Q.; Trinder, C.J.; Peng, L.; Lei, T. Mapping landslide susceptibility at the Three Gorges Reservoir, China, using gradient boosting decision tree, random forest and information value models. *J. Mt. Sci.* **2020**, *17*, 670–685. [CrossRef]
16. Guzzetti, F.; Reichenbach, P.; Ardizzone, F.; Cardinali, M.; Galli, M. Estimating the quality of landslide susceptibility models. *Geomorphology* **2006**, *81*, 166–184. [CrossRef]
17. Hong, H.; Liu, J.; Zhu, A.X. Modeling landslide susceptibility using LogitBoost alternating decision trees and forest by penalizing attributes with the bagging ensemble. *Sci. Total Environ.* **2020**, *718*, 137231. [CrossRef]
18. Li, W.B.; Fan, X.M.; Huang, F.M.; Wu, X.; Yin, K.; Chang, Z.L. Uncertainties of landslide susceptibility modeling under different environmental factor connections and prediction models. *Earth Sci.* **2021**, *46*, 3777–3795.
19. Pham, B.T.; Phong, T.V.; Nguyen-Thoi, T.; Parial, K.; KSingh, S.; Ly, H.B.; Nguyen, K.T.; Ho, L.S.; Le, H.V.; Prakash, I. Ensemble modeling of landslide susceptibility using random subspace learner and different decision tree classifiers. *Geocarto Int.* **2022**, *37*, 735–757. [CrossRef]

20. Segoni, S.; Tofani, V.; Rosi, A.; Catani, F.; Casagli, N. Combination of rainfall thresholds and susceptibility maps for dynamic landslide hazard assessment at regional scale. *Front. Earth Sci.* **2018**, *6*, 85. [CrossRef]
21. Kalantar, B.; Ueda, N.; Saeidi, V.; Ahmadi, K.; Halin, A.A.; Shabani, F. Landslide susceptibility mapping: Machine and ensemble learning based on remote sensing big data. *Remote Sens.* **2020**, *12*, 1737. [CrossRef]
22. Hu, X.; Mei, H.; Zhang, H.; Li, Y.; Li, M. Performance evaluation of ensemble learning techniques for landslide susceptibility mapping at the Jinping county, Southwest China. *Nat. Hazards* **2020**, *105*, 1663–1689. [CrossRef]
23. Santangelo, M.; RMarchesini, I.; Bucci, F.; Cardinali, M.; Cavalli, M.; Crema, S.; Marchi, L.; Alvioli, M.; Guzzetti, F. Exposure to landslides in rural areas in Central Italy. *J. Maps* **2021**, *17*, 124–132. [CrossRef]
24. Ciampalini, A.; Raspini, F.; Lagomarsino, D.; Catani, F.; Casagli, N. Landslide susceptibility map refinement using PSInSAR data. *Remote Sens. Environ.* **2016**, *184*, 302–315. [CrossRef]
25. Dai, C.; Li, W.; Lu, H.; Zhang, S. Landslide hazard assessment method considering the deformation factor: A case study of Zhouqu, Gansu Province, Northwest China. *Remote Sens.* **2023**, *15*, 596. [CrossRef]
26. Roy, P.; Martha, T.R.; Khanna, K.; Jain, N.; Kumar, K.V. Time and path prediction of landslides using InSAR and flow model. *Remote Sens. Environ.* **2022**, *271*, 112899. [CrossRef]
27. van Natijne, A.; Bogaard, T.; van Leijen, F.; Hanssen, R.; Lindenbergh, R. World-wide InSAR sensitivity index for landslide deformation tracking. *Int. J. Appl. Earth Obs. Geoinf.* **2022**, *111*, 102829. [CrossRef]
28. Dong, J.; Niu, R.; Li, B.; Xu, H.; Wang, S. Potential landslides identification based on temporal and spatial filtering of SBAS-InSAR results. *Geomat. Nat. Hazards Risk* **2023**, *14*, 52–75. [CrossRef]
29. Dong, L.; Wang, C.; Tang, Y.; Tang, F.; Zhang, H.; Wang, J.; Duan, W. Time series InSAR three-dimensional displacement inversion model of coal mining areas based on symmetrical features of mining subsidence. *Remote Sens.* **2021**, *13*, 2143. [CrossRef]
30. Ponziani, F.; Ciuffi, P.; Bayer, B.; Berni, N.; Franceschini, S.; Simoni, A. Regional-scale InSAR investigation and landslide early warning thresholds in Umbria, Italy. *Eng. Geol.* **2023**, *327*, 107352. [CrossRef]
31. Devara, M.; Tiwari, A.; Dwivedi, R. Landslide susceptibility mapping using MT-InSAR and AHP enabled GIS-based multi-criteria decision analysis. *Geomat. Nat. Hazards Risk* **2021**, *12*, 675–693. [CrossRef]
32. Cao, C.; Zhu, K.; Xu, P.; Shan, B.; Yang, G.; Song, S. Refined landslide susceptibility analysis based on InSAR technology and UAV multi-source data. *J. Clean. Prod.* **2022**, *368*, 133146. [CrossRef]
33. Liu, W.; Zhang, Y.; Liang, Y.; Sun, P.; Li, Y.; Su, X.; Wang, A.; Meng, X. Landslide risk assessment using a combined approach based on InSAR and random forest. *Remote Sens.* **2022**, *14*, 2131. [CrossRef]
34. Hong, H. Assessing landslide susceptibility based on hybrid Best-first decision tree with ensemble learning model. *Ecol. Indic.* **2023**, *147*, 109968. [CrossRef]
35. Kouhartsiouk, D.; Perdikou, S. The application of DInSAR and Bayesian statistics for the assessment of landslide susceptibility. *Nat. Hazards* **2021**, *105*, 2957–2985. [CrossRef]
36. Xiao, B.; Zhao, J.; Li, D.; Zhao, Z.; Zhou, D.; Xi, W.; Li, Y. Combined SBAS-InSAR and PSO-RF Algorithm for Evaluating the Susceptibility Prediction of Landslide in Complex Mountainous Area: A Case Study of Ludian County, China. *Sensors* **2022**, *22*, 8041. [CrossRef] [PubMed]
37. Zhang, W.; Wu, C.; Tang, L.; Gu, X.; Wang, L. Efficient time-variant reliability analysis of Bazimen landslide in the Three Gorges Reservoir Area using XGBoost and LightGBM algorithms. *Gondwana Res.* **2023**, *123*, 41–53. [CrossRef]
38. Sun, D.; Gu, Q.; Wen, H.; Xu, J.; Zhang, Y.; Shi, S.; Xue, M.; Zhou, X. Assessment of landslide susceptibility along mountain highways based on different machine learning algorithms and mapping units by hybrid factors screening and sample optimization. *Gondwana Res.* **2023**, *123*, 89–106. [CrossRef]
39. Cemiloglu, A.; Zhu, L.; Mohammednour, A.B.; Azarafza, M.; Nanehkaran, Y.A. Landslide susceptibility assessment for Maragheh County, Iran, using the logistic regression algorithm. *Land* **2023**, *12*, 1397. [CrossRef]
40. Yang, C.; Liu, L.-L.; Huang, F.; Huang, L.; Wang, X.-M. Machine learning-based landslide susceptibility assessment with optimized ratio of landslide to non-landslide samples. *Gondwana Res.* **2023**, *123*, 198–216. [CrossRef]
41. Sameen, M.I.; Pradhan, B.; Bui, D.T.; Alamri, A.M. Systematic sample subdividing strategy for training landslide susceptibility models. *Catena* **2020**, *187*, 104358. [CrossRef]
42. Cheng, W.; Zhu, J.; Zeng, X.; You, Y.; Li, X.; Wu, J. Water Resources Carrying Capacity Based on the DPSIRM Framework: Empirical Evidence from Shiyan City, China. *Water* **2023**, *15*, 3060. [CrossRef]
43. Sheng, Y.; Xu, G.; Jin, B.; Zhou, C.; Li, Y.; Chen, W. Data-driven landslide spatial prediction and deformation monitoring: A case study of Shiyan City, China. *Remote Sens.* **2023**, *15*, 5256. [CrossRef]
44. Fu, Z.; Zhang, Y.; Jing, X.; Wang, S.; Zhao, L. Spatial nutrient load analysis based on output coefficient method and land use pattern identification: A case study of Shiyan City. *J. Environ. Eng. Technol.* **2022**, *12*, 660–665.
45. Zhu, Z.; Chen, L.; Zhou, L.; Zhou, Y.; Li, J.; Luo, J.; Xiao, S.; Gao, Q. Surface Deformation Monitoring in Shiyan Based on Multi-Temporal Insar Technology. *ISPRS Ann. Photogramm. Remote Sens. Spat. Inf. Sci.* **2023**, *10*, 755–761. [CrossRef]
46. Khan, H.; Shafique, M.; Khan, M.A.; Bacha, M.A.; Shah, S.U.; Calligaris, C. Landslide susceptibility assessment using Frequency Ratio, a case study of northern Pakistan. *Egypt. J. Remote. Sens. Space Sci.* **2018**, *22*, 11–24. [CrossRef]
47. Kumar, A.; Sharma, R.K.; Bansal, V.K. GIS-based comparative study of information value and frequency ratio method for landslide hazard zonation in a part of mid-Himalaya in Himachal Pradesh. *Innov. Infrastruct. Solut.* **2019**, *4*, 28. [CrossRef]

48. Yan, Y.; Doin, M.-P.; Lopez-Quiroz, P.; Tupin, F.; Fruneau, B.; Pinel, V.; Trouve, E. Mexico City subsidence measured by InSAR time series: Joint analysis using PS and SBAS approaches. *IEEE J. Sel. Top. Appl. Earth Obs. Remote Sens.* **2012**, *5*, 1312–1326. [CrossRef]
49. Zhang, G.; Wang, S.; Chen, Z.; Liu, Y.; Xu, Z.; Zhao, R. Landslide susceptibility evaluation integrating weight of evidence model and InSAR results, west of Hubei Province, China. *Egypt. J. Remote Sens. Space Sci.* **2023**, *26*, 95–106. [CrossRef]
50. Li, S.; Xu, W.; Li, Z. Review of the SBAS InSAR Time-series algorithms, applications, and challenges. *Geod. Geodyn.* **2022**, *13*, 114–126. [CrossRef]
51. Chen, Y.; Tong, Y.; Tan, K. Coal mining deformation monitoring using SBAS-InSAR and offset tracking: A case study of Yu County, China. *IEEE J. Sel. Top. Appl. Earth Obs. Remote Sens.* **2020**, *13*, 6077–6087. [CrossRef]
52. Zhang, Z.; Hu, C.; Wu, Z.; Zhang, Z.; Yang, S.; Yang, W. Monitoring and analysis of ground subsidence in Shanghai based on PS-InSAR and SBAS-InSAR technologies. *Sci. Rep.* **2023**, *13*, 8031. [CrossRef]
53. Liu, Y.; Yang, H.; Wang, S.; Xu, L.; Peng, J. Monitoring and stability analysis of the deformation in the Woda landslide area in Tibet, China by the DS-InSAR method. *Remote Sens.* **2022**, *14*, 532. [CrossRef]
54. Liu, G.; Zbigniew, P.; Stefano, S.; Benni, T.; Wu, L.; Fan, J.; Bai, S.; Wei, L.; Yan, S.; Song, R.; et al. Land surface displacement geohazards monitoring using multi-temporal InSAR techniques. *J. Geod. Geoinf. Sci.* **2021**, *4*, 77.
55. Awasthi, S.; Jain, K.; Bhattacharjee, S.; Gupta, V.; Varade, D.; Singh, H.; Narayan, A.B.; Budillon, A. Analyzing urbanization induced groundwater stress and land deformation using time-series Sentinel-1 datasets applying PSInSAR approach. *Sci. Total Environ.* **2022**, *844*, 157103. [CrossRef]
56. Zhu, Z.; Gan, S.; Yuan, X.; Zhang, J. Landslide susceptibility mapping with integrated SBAS-InSAR technique: A case study of Dongchuan District, Yunnan (China). *Sensors* **2022**, *22*, 5587. [CrossRef] [PubMed]
57. Jiao, W.; Wang, L.; McCabe, M.F. Multi-sensor remote sensing for drought characterization: Current status, opportunities and a roadmap for the future. *Remote Sens. Environ.* **2021**, *256*, 112313. [CrossRef]
58. Kang, Y.; Lu, Z.; Zhao, C.; Xu, Y.; Kim, J.W.; Gallegos, A.J. InSAR monitoring of creeping landslides in mountainous regions: A case study in Eldorado National Forest, California. *Remote Sens. Environ.* **2021**, *258*, 112400. [CrossRef]
59. Rana, K.; Ozturk, U.; Malik, N. Landslide geometry reveals its trigger. *Geophys. Res. Lett.* **2021**, *48*, e2020GL090848. [CrossRef]